

On the Deconfinement Phase Transition in Neutron-Star Mergers

Elias R. Most^{1,2}, L. Jens Papenfort¹, Veronica Dexheimer³, Matthias Hanauske^{1,4}, Horst Stoecker^{1,4,5}, and Luciano Rezzolla^{1,6}

¹ Institut für Theoretische Physik, Max-von-Laue-Straße 1, 60438 Frankfurt, Germany

² Center for Computational Astrophysics, Flatiron Institute, 162 Fifth Avenue, New York, NY 10010, USA

³ Department of Physics, Kent State University, Kent, OH 44243 USA

⁴ Frankfurt Institute for Advanced Studies, Ruth-Moufang-Straße 1, 60438 Frankfurt, Germany

⁵ GSI Helmholtzzentrum für Schwerionenforschung GmbH, 64291 Darmstadt, Germany

⁶ School of Mathematics, Trinity College, Dublin 2, Ireland

Received: date / Revised version: date

Abstract. We study in detail the nuclear aspects of a neutron-star merger in which deconfinement to quark matter takes place. For this purpose, we make use of the Chiral Mean Field (CMF) model, an effective relativistic model that includes self-consistent chiral symmetry restoration and deconfinement to quark matter and, for this reason, predicts the existence of different degrees of freedom depending on the local density/chemical potential and temperature. We then use the out-of-chemical-equilibrium finite-temperature CMF equation of state in full general-relativistic simulations to analyze which regions of different QCD phase diagrams are probed and which conditions, such as strangeness and entropy, are generated when a strong first-order phase transition appears. We also investigate the amount of electrons present in different stages of the merger and discuss how far from chemical equilibrium they can be and, finally, draw some comparisons with matter created in supernova explosions and heavy-ion collisions.

PACS. PACS-key describing text of that key – PACS-key describing text of that key

1 Introduction

The interior of neutron stars covers an incredible range of densities going from about 10^4 g/cm³ in the crust to about 10^{15} g/cm³ in the core, corresponding to several times the nuclear saturation density [1]. During a neutron-star merger this value can increase to several times 10^{15} g/cm³ in the center, corresponding to more than 10 times the nuclear saturation density (see Refs. [2; 3] for some recent reviews). Such extreme densities combined with temperatures of several tens of MeV are particularly relevant if the equation of state (EOS) allows for a deconfinement to quark matter takes place [4; 5; 6]. Clearly, the investigation of these scenarios requires, from one hand, the use of accurate numerical-relativity calculations and, from the other hand, a microscopic description that allows for the existence exotic degrees of freedom, such as hyperons and quarks (see Ref. [7] for a review of the relation between gravitational waves and the microscopic description of neutron stars).

It has been shown in Refs. [8; 9] that hyperons can modify the frequency and amplitude of gravitational waves emitted by neutron-star mergers. These changes are ex-

pected to be visible even before the merger takes place, as hyperons are usually triggered at intermediate densities, specially when temperature effects are pronounced. Deconfinement to quark matter, on the other hand, was found to modify the frequency and amplitude of gravitational waves emitted only at [6] or after the merger [5]. The possibility of the merger of pure quark stars have also investigated in the past [10]. More recently, attention has been paid to the merger of twin stars in terms of equilibrium models [11; 12] or through simulations in full general relativity of the merger of a hadronic and a quark star [13] and quark stars with hadronic crusts [14]. In a holographic approach, Ref [15] has found not to be possible to reach the phase transition to the quark phase before collapsing to a black hole. The complex dynamics found in these works, as well as the impact on the electromagnetic counterpart to be expected from this process [16], clearly calls for more extended and detailed work.

It has been shown that a deconfinement phase transition can produce shock waves in stars [17]. In a previous work [5], we reported that a strong first-order phase transition to quark matter can lead to a post-merger gravitational-wave signal that is different from the one expected from the inspiral, which can only probe the hadronic part of

Send offprint requests to:

the EOS. In particular, within the scenario investigated in Ref. [5], small amounts of quarks in hot regions of the hypermassive neutron star (HMNS) lead to a dephasing of the signal, while the appearance of a strong first-order phase transition induces an early collapse of the remnant to a black hole, producing a ringdown signal which is different from the collapse of a purely hadronic remnant. Here, we provide a number of additional pieces of information and expand on the analysis carried out in Ref. [5]. In particular, we here focus on the nuclear aspects of a merger event in which a deconfinement phase transition takes place in order to understand how the outcome compares to matter generated in core-collapse supernova explosions or in heavy-ion collisions. For this, we analyze the light and strange-quark content at the time when a hot quark-phase is formed in the HMNS. We also show what thermodynamical conditions, such as temperature and entropy, and compositions (charge, lepton, and strangeness fractions) are generated and which baryon, charge, and electron chemical potentials they correspond to. This can serve as a guide for nuclear physicists who want to study the effects of neutron-star merger conditions in their EOSs that contain exotic degrees of freedom.

The plan of the paper is as follows: first, we discuss the microscopic EoS and the hydrodynamical code used for the merger simulation. Then, we present the outcome of our simulations and discuss our results. Finally, we compare our findings with other hot and dense environments and present our conclusions.

2 Methods

2.1 Equation of state

Due to the extreme conditions expected to be found in neutron-star mergers, it is compelling to construct the EOS applying a formalism that includes the basic features predicted by QCD, namely chiral-symmetry restoration and quark deconfinement. In the absence of a fundamental theory that can be applied in the whole energy regime and conditions necessary for our study, we make use of an effective model, the Chiral Mean Field (CMF) model, which is based on a nonlinear realization of the SU(3) chiral sigma formalism [18]. It is a relativistic model constructed from symmetry relations, which allows it to be chirally invariant in the expected regime. The baryon and quark masses are generated by interactions with the medium and, therefore, decrease with temperature and/or chemical potential/density. The Lagrangian density of the CMF model in the mean field approximation reads [19; 20]

$$L = L_{\text{kin}} + L_{\text{int}} + L_{\text{self}} + L_{\text{sb}} - U, \quad (1)$$

where, besides the kinetic energy term for hadrons, quarks and electrons (L_{kin}), the terms remaining correspond to the interaction between the octet of baryons with spin 1/2, the 3 lighter quarks, and mesons (L_{int}), self interactions of scalar and vector mesons (L_{self}), an explicit chiral symmetry breaking term necessary to produce vacuum masses for

the pseudo-scalar mesons (L_{sb}), and the effective potential U for the scalar field Φ . This scalar field was named in an analogy to the Polyakov loop in the (Polyakov) Nambu and Jona-Lasinio (PNJL) approach [21; 22] and its potential in our approach depends on the temperature T and the baryon chemical potential μ_B

$$U = (a_0 T^4 + a_1 \mu_B^4 + a_2 T^2 \mu_B^2) \Phi^2 + a_3 T_0^4 \ln(1 - 6\Phi^2 + 8\Phi^3 - 3\Phi^4). \quad (2)$$

The mesons included are the vector-isoscalars ω and ϕ (strange quark-antiquark state), the vector-isovector ρ , the scalar-isoscalars σ and ζ (also strange quark-antiquark state), and the scalar-isovector δ . They are treated as classical fields within the mean-field approximation. Finite-temperature calculations include the heat bath of hadronic and quark quasiparticles within the grand canonical ensemble. The grand potential density of the system is defined as

$$\frac{\Omega}{V} = -L_{\text{int}} - L_{\text{self}} - L_{\text{sb}} - L_{\text{vac}} + U + T \sum_i \frac{\gamma_i}{(2\pi)^3} \int_0^\infty d^3k \ln(1 + e^{-\frac{1}{T}(E_i^*(k) \mp \mu_i^*)}), \quad (3)$$

where L_{vac} is the vacuum energy, γ_i is the fermionic degeneracy (which for the quarks also includes color degeneracy), $E_i^*(k) = \sqrt{k_i^2 + M_i^{*2}}$, is the single particle effective energy and

$$\mu_i^* = \mu_i - g_{i\omega}\omega - g_\phi\phi - g_{i\rho}\tau_3\rho, \quad (4)$$

is the effective chemical potential of each species. The $-$ and $+$ signs in the grand potential density (3) refer to particles and antiparticles, respectively. The chemical potential for each species μ_i is determined by the conditions imposed to the system, conserved baryon number and electric charge,

$$\mu_i = Q_{B,i} \mu_B + Q_i \mu_Q, \quad (5)$$

where μ_B and μ_Q represent the chemical potentials corresponding to the conserved quantities and the values $Q_{B,i}$ and Q_i are the baryon charge (1 for baryons and 1/3 for quarks) and electric charge of a particular species i .

The coupling constants of the hadronic sector of the model were fitted to reproduce vacuum masses of baryons and mesons, nuclear saturation properties (density $\rho_0 = 0.15 \text{ fm}^{-3}$, binding energy per nucleon $B/A = -16 \text{ MeV}$, and compressibility $K = 300 \text{ MeV}$), the asymmetry energy ($E_{\text{sym}} = 30 \text{ MeV}$ with slope $L = 88 \text{ MeV}$), and reasonable values for the hyperon potentials ($U_\Lambda = -28.00 \text{ MeV}$, $U_\Sigma = 5 \text{ MeV}$, and $U_\Xi = -18 \text{ MeV}$). The reproduced critical point for the nuclear liquid-gas phase transition lies at $T_c = 16.4 \text{ MeV}$, $\mu_{B,c} = 910 \text{ MeV}$, while the vacuum expectation values of the scalar mesons are constrained by reproducing the pion and kaon decay constants.

Due to their interactions with the mean field of mesons and the field Φ , the effective masses of baryons and quarks

take the following form in our approach

$$M_B^* = g_{B\sigma}\sigma + g_{B\delta}\tau_3\delta + g_{B\zeta}\zeta + M_{0_B} + g_{B\Phi}\Phi^2, \quad (6)$$

$$M_q^* = g_{q\sigma}\sigma + g_{q\delta}\tau_3\delta + g_{q\zeta}\zeta + M_{0_q} + g_{q\Phi}(1 - \Phi), \quad (7)$$

where M_0 are small bare-mass terms. Notice that for low values of Φ , M_B^* is small while M_q^* is very large. This essentially indicates that, for low Φ , the presence of baryons is promoted while quarks are suppressed, and vice versa. In this sense, Φ acts as an order parameter for deconfinement. The potential U , together with the quark couplings, has been fit to reproduce several features expected from the QCD phase diagram, including lattice data for pure gauge and with quarks (procedure explained in detail in Ref. [20]). In the latter case, we reproduce a crossover at vanishing and small chemical potential, after which a first-order coexistence line starts, continuing all the way to the zero temperature axis. The values of all coupling constants can be found in Ref. [23].

It should be mentioned that the CMF model allows for the existence of soluted quarks in the hadronic phase and soluted hadrons in the quark phase at finite temperature. This is different from a Gibbs construction and the appearance of mixture of phases, which eliminates discontinuities in the first derivatives of the grand potential (see Refs. [24; 25; 26; 27] and Ref. [28] with references therein for details). Regardless, quarks always give the dominant contribution in the quark phase, and hadrons in the hadronic phase. We assume that this inter-penetration of quarks and hadrons is indeed physical, and is required to achieve the crossover transition, known to take place at low μ_B values [29].

For cold chemically equilibrated matter, the formalism leads to a neutron star with maximum mass of $2.07 M_\odot$ and a radius of 12 km when quarks are suppressed. Otherwise, the model presents a very strong deconfinement phase transition that destabilizes stars (as no quark-vector interactions are included in agreement with lattice QCD [30]), unless a mixtures of phases is allowed. In the latter case, we reproduce a stable maximum-mass star with $1.93 M_\odot$ and a radius of 13 km [23], more than 2 km of which contain quarks. For the canonical star with mass $1.4 M_\odot$, a corresponding radius of 14 km is found. In addition, when we consider nonlinear isovector singlet to isovector triplet coupling of the vector mesons for the baryons, the radius of the $1.4 M_\odot$ star reduces to less than 13 km [31]. These values of the maximum mass and radii are compatible with the expectations matured after the first detection of gravitational waves from a binary neutron-star merger (GW170817) [32; 33; 34; 35; 36; 37; 38; 39; 40]. For pro-neutron stars, we reproduce a stable maximum-mass star with $2.03 M_\odot$ and a radius of 18 km, more than 7 km of which contain quarks [23].

In order to use our microscopic formalism in neutron-star merger simulations, we build 3-dimensional tables in which we vary the baryon number density, charge fraction, and temperature. The baryon number density is defined as

$$n_B = - \left. \frac{\partial \Omega / V}{\partial \mu_B} \right|_{T, V, \mu_Q} = \sum_i n_i - \frac{\partial U}{\partial \mu_B}, \quad (8)$$

where n_i is the number density of particle species i . The extra contribution of the gluons to the baryon density represents color bound states and mimics extra possible states, as for example the contribution of higher resonances.

The charge fraction is calculated as the amount of electric charge per baryon (and quark) and it is only summed over baryons and quarks

$$Y_Q = \frac{Q}{B} = \frac{\sum_i Q_i n_i}{\sum_i Q_{B,i} n_i}. \quad (9)$$

The electrons, which are not considered to be in chemical equilibrium with the rest of the system, are then added in order to fulfill electric charge neutrality

$$n_e = - \sum_i Q_i n_i = Y_Q \sum_i Q_{B,i} n_i. \quad (10)$$

In Ref. [41], it was described in detail the construction of the three-dimensional table, which is already available online on the CompOSE repository [42; 43] for hadronic matter. In the future, equivalent tables but that also contain quark degrees of freedom will be uploaded. Figures (3) and (4) of Ref. [41] show the effect of the increase of charge fraction in the CMF model. At zero temperature, going from $Y_Q = 0$ to $Y_Q = 0.5$ essentially eliminates hyperons and pushes strange quarks to densities that are too high to be important for cold neutron stars.

2.2 Numerical infrastructure

For completeness, we quickly summarize the numerical methods used for the simulations reported here and first discussed in Ref. [5]. More specifically, we solve a coupled system of the Einstein and general-relativistic magnetohydrodynamics (GRMHD) equations using the code `Frankfurt/IllinoisGRMHD` (FIL), which is a high-order extension of the publicly available `IllinoisGRMHD` code [44] part of the `Einstein Toolkit` [45]. In the following, we give an overview of the numerical details and implementation of the formalism.

To solve the Einstein equations, FIL provides its own spacetime evolution module, which implements the Z4c [46; 47] and CCZ4 [48; 49] formulations using forth-order accurate finite differencing [50] with different choices for the conformal factor. In this work, we choose ψ^{-2} and adopt the Z4c formulation with a damping coefficient $\kappa = 0.02$ [51; 46]. The space-time gauges are evolved using the standard 1+log slicing and shifting-shift Gamma driver conditions [52; 53], where a uniform damping parameter of $\eta = 2/M$ is adopted.

The GRMHD equations are solved using the ECHO scheme [54], making our code overall formally fourth-order accurate. The fluxes are computed from the reconstructed primitive variables using a HLLC Riemann solver [55]. The reconstruction step \mathcal{R} is performed using the WENO-Z method [56], with the optimal weights and stencils for a conservative finite difference scheme taken from Ref. [54].

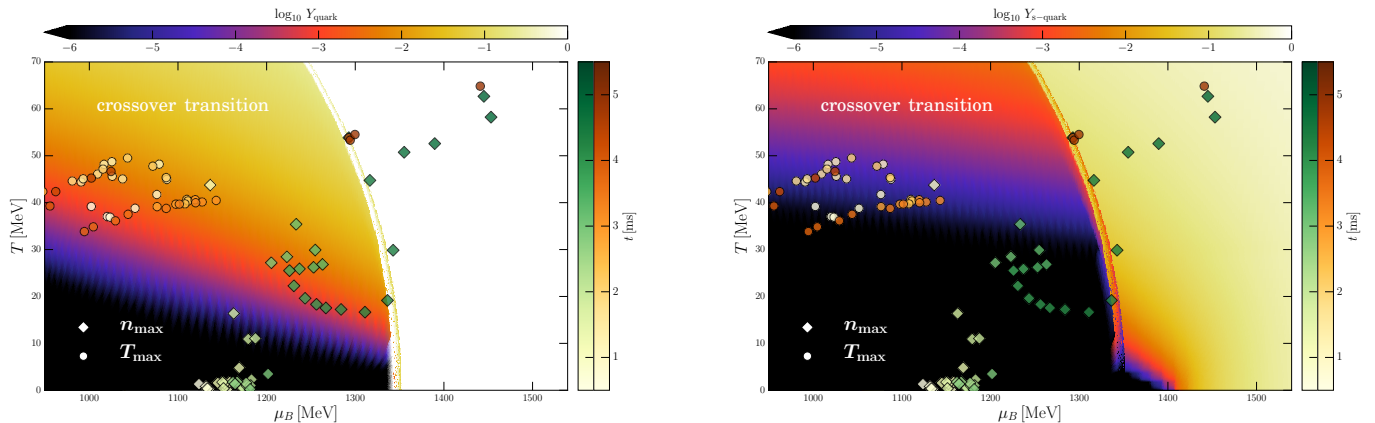


Fig. 1. *Left panel:* Evolution of the densest and hottest parts of the hypermassive neutron star in the QCD phase diagram. The background color refers to the total quark fraction predicted by the CMF model for charge fraction $Y_Q = 0.05$. The different symbols describe the evolution of the largest baryon density and largest temperature points encountered during the simulation. *Right panel:* Same as in the left panel, but showing in the background the strange-quark fraction predicted by the CMF model for charge fraction $Y_Q = 0.05$.

Our initial data is represented by an irrotational equal-mass neutron star binary with a total mass of $2.9 M_\odot$ constructed using the LORENE code having an initial proper separation of 45 km. The simulation domain is modeled by a series of seven nested boxes extending up to $\simeq 1500$ km for which the finest-grid box has a resolution of 250 m.

3 Results

We start by analyzing the evolution of the densest and hottest parts of the HMNS in the left panel of Fig. 1, which reports the regions of the standard QCD phase diagram (temperature vs. baryon chemical potential) that are probed in our neutron-star merger simulation. In particular, we show with a color-code in the background of the figure the quark fraction Y_{quark} (i.e., the number of quarks normalized by the total number of baryons and quarks B) predicted by CMF model when the charge fraction for the baryons and quarks is fixed to $Y_Q = 0.05$. This is a good approximation for the charge fraction present at intermediate densities when the merger event starts (see discussion below for Fig. 3). As expected from our formalism, the phase transition is quite sharp at zero and low temperatures, reproducing pure hadronic matter to the left (black region) and pure quark matter to the right (white region) of the coexistence line. On the other hand, the phase transition becomes smoother for larger temperatures to the point that, if we had extended the figure to larger temperatures, the first-order coexistence line would have disappeared before reaching the zero baryon chemical potential axis, at a critical temperature of $T_c = 169$ MeV.

The finite width for the coexistence line in the left panel of Fig. 1 is related to the use of the baryon chemical potential for the horizontal axis, which is not the Gibbs free energy per baryon of the system in the case of a fixed charge fraction. The independent chemical potential and Gibbs free energy per baryon of the system in this case is $\tilde{\mu} = \mu_B + Y_Q \mu_Q$ [28; 42].

The different symbols in Fig. 1 describe the evolution of the largest baryon density and largest temperature points encountered during the simulation. The largest density represented by diamonds corresponds, first, to the reminiscent of the original neutron stars and, later, to the center of the HMNS formed by the merger. As time evolves, these points correspond to larger baryon chemical potentials and, on average, larger temperatures, except for the earlier stage when the densest points switch between the two reminiscent stars. After $\simeq 4.5$ ms, the coexistence line is crossed and a large amount of deconfined quark matter appears in the center of the newly formed HMNS. The hottest region represented by circles on the figure corresponds to different regions of the merger and, only after deconfinement to quark matter takes place, it coincides with the center of the HMNS (brown circles). Before that, the hottest region appears off-center in the shape of a ring [57; 58], mostly as a manifestation of the conservation of the Bernoulli constant [58].

The right panel of Fig. 1 also shows which regions of the standard QCD phase diagram are probed in a neutron-star merger but, now, we show in the background the amount of strange quarks $Y_{\text{s-quark}}$ (number of s-quarks normalized by B) predicted by the CMF model for $Y_Q = 0.05$. Note that strange quarks do not appear immediately after the deconfinement phase transition at low temperatures (black region), a consequence of their large bare mass. Even at intermediate and larger temperatures, the amount of strange quarks is roughly an order of magnitude less than that of up and down quarks combined. Nevertheless, in the final stages of the merger, a combination of large densities and temperatures can produce $Y_{\text{s-quark}} > 10\%$ in the center of the HMNS.

To better highlight the various regions of the phase diagram probed by the HMNS, Fig. 2 shows the temperature and baryon chemical potential values covered at a fiducial time when the quark phase has already formed after the merger, about 5 ms for the case a total mass of

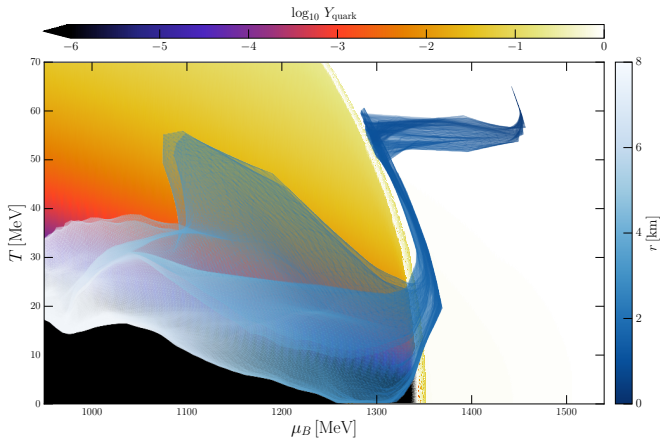


Fig. 2. Portion of the QCD phase diagram covered by the simulation immediately after deconfinement to quark matter has taken place in its center. The background color is the same as in the left panel of Fig. 1. The blue scale shows the distance to the center of the hypermassive neutron star.

$2.9 M_{\odot}$. The blue color code shows the distance to the center of the HMNS up to 8 km of radius. We can see that the hadronic part of the HMNS covers a large area of the phase diagram extending up to $T > 55$ MeV [59; 60]. In the region where the deconfinement takes place, there is a large temperature increase related to the gravitational collapse due to the softening of the EoS across the first-order phase transition, the latter having already being shown in the horizontal axis of Fig. 3 of Ref. [5]. Note that our deconfinement phase transition is not an adiabatic process. During this stage, even if the temperature was kept constant, the entropy S_B would increase by a factor ~ 3 , related to the appearance of color degrees of freedom and different interactions in the quark phase. In the deconfined phase, the temperature reaches even larger values $T \simeq 60$ MeV. Beyond the rightmost point of the phase diagram, an apparent horizon starts to form and, as the simulation proceeds, the HMNS collapses to black hole in a few ms.

Note that the time-averaged charge fraction measured during the whole simulation is larger than $Y_Q = 0.05$, as shown in the left panel of Fig. 3. This panel is similar to the left panel Fig. 1, in the sense that it also follows the evolution of the densest and hottest points of the merger simulation, but it relates the charge fraction and the baryon chemical potential. Overall, the charge fraction achieved is larger for larger chemical potentials, going up to $Y_Q \simeq 0.12$, right before the temperature starts to increase. When this happens, Y_Q drops as a result of the appearance of the quarks (medium-green diamonds). This occurs before the phase transition takes place for the densest points. For the hottest points, Y_Q increases at the deconfinement phase transition (orange to brown circles), beyond which they they correspond to the stellar center.

Since electric charge neutrality is always required for stellar stability, the charge density of electrons has to bal-

ance the charge density of baryons and quarks. As a consequence, the lepton fraction Y_e , defined as the number of electrons over the number of baryons and quarks, is the same as the charge fraction

$$Y_e = \frac{L}{B} = \frac{n_e}{\sum_i Q_{B,i} n_i} = \frac{\sum_i Q_i n_i}{\sum_i Q_{B,i} n_i} = Y_Q. \quad (11)$$

It was found in Ref. [61] using several hadronic equations of state that the electron fraction does not go above $Y_e = 0.12$ in neutron star mergers, the same limiting value we obtained.

The right panel of Fig. 3 again follows the evolution of the densest and hottest points of the merger simulation, but now relates the charged chemical potential and the baryon chemical potential. It is interesting to note that, separately in each phase, the relation between the two quantities is approximately linear (the light-green diamonds present a slightly different slope because they represent a cold region with no quarks). The very different slopes at different times (top and bottom of panel) stem from the fact that the charged chemical potential increases (in absolute value) with density much faster in the hadronic phase than in the quark one. This behaviour has already been shown in Ref. [23] for both charged and lepton chemical potentials for the particular case of fixed temperature and in chemical equilibrium. The jump from the bottom to the top line points to the first-order deconfinement transition that takes place in the simulation.

Next, we concentrate again on a specific (same as in Fig. 2) time during the simulation after the deconfinement to quark matter has taken place to discuss how the different chemical potentials are spatially distributed within the HMNS. The contours in Figs. 4–6 refer to values of the rest-mass density boundaries between $10^{12} - 10^{15}$ g/cm³, the latter being equivalent to 0.6 fm⁻³. The left part of Fig. 4 shows the charged chemical potential. It can be seen how it increases (in absolute value) with density towards the center of the HMNS until the phase transition takes place, when it decreases rapidly (in absolute value). The right part of Fig. 4, on the other hand, reports the electron chemical potential and shows that it increases (on average) toward the center of the HMNS, being almost not sensitive to the deconfinement phase transition. The difference between these two quantities can be seen as a measure of the distance from chemical equilibrium, when by construction $\mu_e = -\mu_Q$.

At zero temperature, we can use the definition of the number density $n_i = (\gamma_i/6\pi^2)k_{F_i}^3$ and of the Fermi momentum $k_{F_i} = \sqrt{(\mu_i + \text{vec}^2 - M_i^{*2})}$, together with Eqs. (5) and (11) to write a general relation connecting electron and charged chemical potential

$$\mu_e = \left[\left(\sum_i \frac{\gamma_i}{\gamma_e} Q_i [(Q_{B,i} \mu_B + Q_i \mu_Q + \text{vec})^2 - M_i^{*2}]^{3/2} \right)^{2/3} + m_e^2 \right]^{1/2}. \quad (12)$$

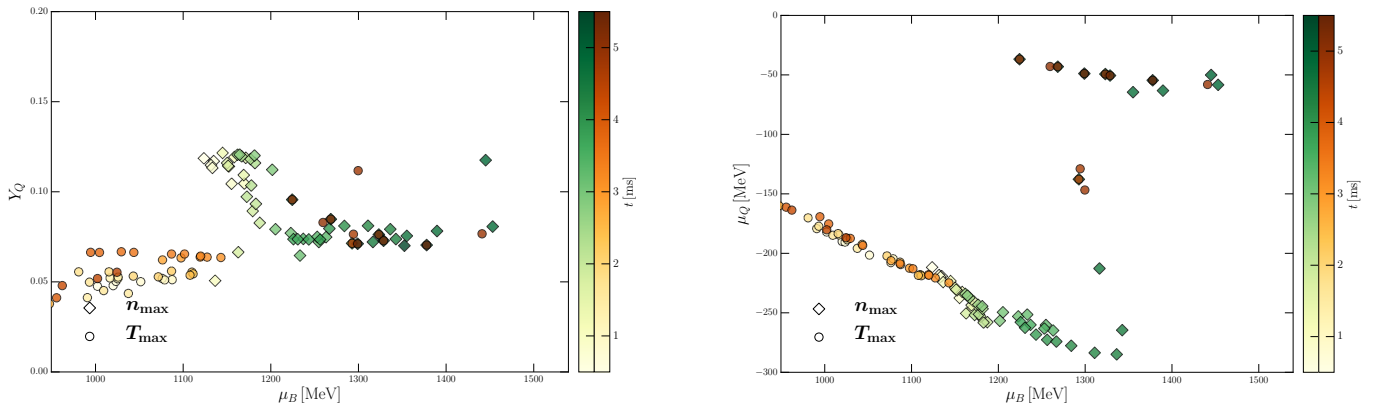


Fig. 3. *Left panel:* The charge fraction vs. baryon chemical potential phase diagram. The symbols once more follow the densest and hottest points of the hypermassive neutron star. *Right panel:* Same as in the left panel but for the charged chemical potential.

We used “vec” referring to general vector interactions, but they are specified in Eq. (4) for our model. In the case in which both quark and hyperon degrees of freedom are suppressed, the expression above reduces to

$$\mu_e = \left[(\mu_B + \mu_Q + \text{vec})^2 - M_p^{*2} + m_e^2 \right]^{1/2}. \quad (13)$$

The left part of Fig. 5 shows how the entropy density per baryon number density $S_B = s/n_B$ is distributed in space inside the HMNS at the same time of Fig. 4. On average, it decreases towards the center, reaching values close to $S_B = 1$ right before the deconfinement phase transition takes place, beyond which it increases to $S_B \gtrsim 2.5$. The right part of Fig. 5 shows instead the temperature distribution, highlighting that, at intermediate densities, a hot ring appears around the center of the HMNS (see Ref. [58] for an extended discussion of this feature). More importantly, the center of the HMNS becomes very hot at this point in time, i.e., with temperatures $T > 60$ MeV. This is consequence of the gravitational collapse we already discussed. Globally, the entropy S_B increases as the simulation evolves in time, which is related to the appearance of shock waves that develop due to the large compressions experienced by matter as the HMNS settles. This is in a way similar to the dynamics produced in heavy-ion collisions [62; 63] or in supernova explosions [64].

The amount and location of exotic particles (not nucleons) can be seen in Fig. 6 for the same time as in the previous figures. More specifically, the left part reports the baryon and quark strangeness fraction

$$Y_S = \frac{S}{B} = \frac{\sum_i Q_{S_i}}{\sum_i Q_{B,i}}, \quad (14)$$

showing that it increases almost continuously towards the center of the HMNS, reaching $Y_S \simeq 40\%$. This fraction is composed mainly of hyperons until the phase transition, when they are replaced by strange quarks. The right part of Fig. 6 shows how the strange quark fraction is present in low numbers and only in the hot region before the deconfinement transition, but increases reaching $Y_{s\text{-quark}} \simeq 40\%$ in the HMNS center.

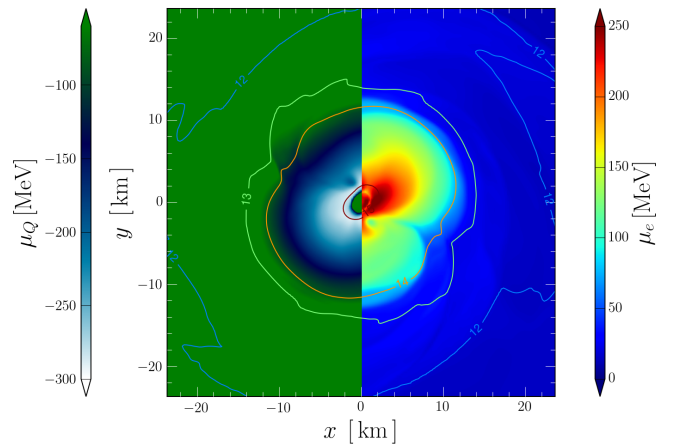


Fig. 4. Snapshot of the hypermassive neutron star immediately after deconfinement to quark matter has taken place in its center showing the charge chemical potential (left part) and electron chemical potential (right part). Contours refer to the rest-mass density.

4 Comparison with other scenarios: supernovae and heavy-ion collisions

The physical conditions discussed so far and potentially encountered after the merger of a binary system of neutron stars could be produced also in two other and different scenarios, namely, supernovae explosions and relativistic heavy-ion collisions.

Right after supernova explosions, the hot and dense medium of young protoneutron stars causes the mean free path of neutrinos to drop dramatically and becoming smaller than the radius of the star [65; 66; 67; 68]. This is usually modeled in nuclear physics assuming a large electron lepton fraction (electron and electron neutrinos) with an electron fraction up to $Y_e = 0.4 (= Y_Q)$, a value obtained from numerical simulations of protoneutron-star evolution [69; 70]. From Fig. 3, it can be seen that the values reached in our merger simulations are much smaller ($\sim 1/3$ of the typical protoneutron-star value), and decrease further

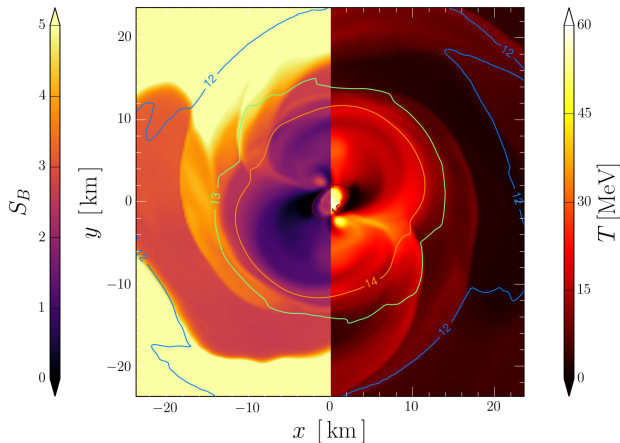


Fig. 5. Same as Fig. 4 but showing entropy density per baryon density (left part) and temperature (right part).

(to $\sim 1/6$ of the proton-neutron-star value in the center of the HMNS after the first-order phase transition has taken place.

Similarly, the temperature evolution in proton-neutron stars is usually approximated by means of a fixed entropy density per baryon number density (or entropy per baryon) S_B . When the entropy per baryon is fixed in a EOS, it allows the temperature to increase almost linearly with density (e.g., towards the stellar center), with typical values of $S_B \simeq 1 - 2$ [65; 71], again as deduced from numerical simulations of proton-neutron-star evolution. Fig. 5 shows that the values reached in our merger simulations are comparable with those typically encountered in proton-neutron-star, being only a bit higher, $S_B = 2.6$, in the region where the first-order phase transition has taken place. Note, however, that in a supernova explosion in which quark deconfinement takes place, the entropy per baryon can be even higher than in our case, reaching $S_B = 3$ [72].

In our simulations, as it is typical of matter in astrophysical scenarios, the net strangeness is nonzero, i.e., amount of strange particles is larger than that of strange antiparticles. This is not the case for matter generated in relativistic heavy-ion collisions, since in this case there is no time for net strangeness to be produced, and a new constraint needs to be added to the formalism $Y_S = 0$ [73; 28]. Note, however, that in a heavy-ion collision large numbers of pions and kaons can escape from the system's surface during the expansion phase, enriching strangeness. As a consequence, at the final chemical freezeout, the strangeness fraction can reach rather high values in the collision core made up of quarks and gluons $Y_S \simeq 0.7$. This is to be contrasted with the maximum value obtained in our merger simulation $Y_S \simeq 0.40$. Notwithstanding this difference and the fact that no electrons are involved in heavy-ion collisions, we draw some rough comparisons. For instance, typical Au-Au and Pb-Pb (and even U) collisions create environments with charge fraction $Y_Q \simeq 0.4$, which is once more much larger than the maximum value produced in our merger simulations, i.e., $Y_Q \simeq 0.12$.

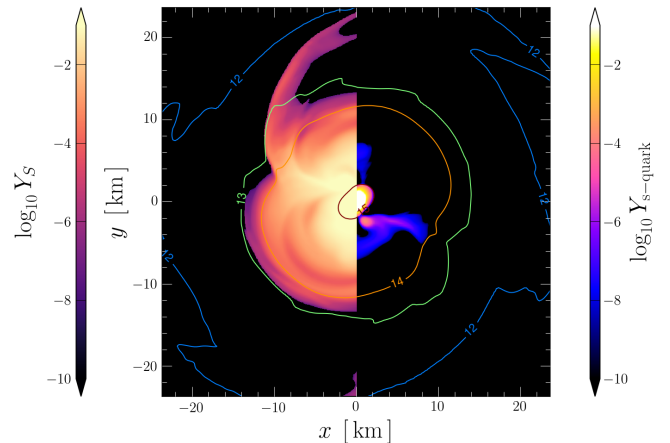


Fig. 6. Same as Fig. 4 but showing strangeness fraction Y_S (left part) and strange-quark fraction $Y_{s\text{-quark}}$ (right part).

Finally, low-energy collisions with energy per nucleon pair $\sqrt{s_{NN}} < 3$ GeV are expected to produce densities of several times saturation density. These densities are even beyond the scope of the second phase of the Beam Energy Scan performed in the Relativistic Heavy Ion Collider at the Brookhaven National Laboratory (RHIC BES-II), but will be the focus of the Facility for Antiproton and Ion Research at the Gesellschaft für Schwerionenforschung in Germany (GSI FAIR) and the Nuclotron-Based Ion Collider Facility in Russia (NICA). In particular, energies per nucleon pair of $\sqrt{s_{NN}} = 2.2, 2.4, 2.6$ GeV are expected to generate initial-state temperatures of $T = 60, 70, 80$ MeV, respectively, hence, corresponding to entropies per baryon of $S_B = 3, 3.5, 4$ (see Tab. II and discussion in Ref. [74] for details). Some of these temperatures and entropies are comparable or only marginally above what we found in our merger simulations.

5 Discussion and conclusions

We have recently presented the first fully general-relativistic simulations showing that quark deconfinement can generate observable signatures in the gravitational waveforms from merging neutron-star binaries [5]. In order to better understand the details and the impacts of the deconfinement first-order phase transition, we have discussed here a number of phase diagrams illustrating the properties of the resulting hypermassive neutron star (HMNS) in terms of the evolution of temperature, baryon chemical potential, charged chemical fraction, and charge fraction.

In particular, we have shown which parts of the phase diagram can be probed in a representative neutron-star merger that generates a $\simeq 2.9 M_\odot$ HMNS in which a deconfinement to quark matter takes place and indicated the approximate amounts of light and strange quark fractions that are created in this way. In turn, this has revealed that a considerable amount of strange quarks, i.e., $Y_{s\text{-quark}} \simeq 40\%$, can appear in the hot center of the HMNS after the deconfinement phase transition has taken place. Of course, this does not mean that strangeness is

not present before the actual phase transition, since light quarks can appear in small amounts in earlier stages of the merger. In addition, hyperons, are generated in large amounts before the transition, as a result of the increase in density and temperature. Therefore, even before the deconfinement phase transition, strangeness fraction can reach $Y_S \simeq 40\%$.

Our study has also revealed that the charged fraction achieved in the simulation decreases when the deconfinement takes place, not exceeding $Y_Q \simeq 0.12$. This value is much smaller than that encountered in typical protoneutron star calculations $Y_Q \simeq 0.4$ or the ones present in relativistic heavy-ion collisions, where again $Y_Q \simeq 0.4$. Furthermore, the charged chemical potential decreases (in absolute value) when the transition takes place and does not match the value of the electron chemical potential. This difference highlights the fact that the merged system is far from chemical equilibrium. Very informative are also the spatial distributions of the various thermodynamical quantities at a representative time after the deconfinement phase transition has taken place. We have illustrated that, while the charged chemical potential is reduced dramatically across the phase transition, the chemical potential of the electrons is not affected significantly.

Finally, we note that the study of all these key thermodynamical quantities is useful to validate whether the physical conditions produced in neutron-star mergers are indeed similar to the those generated in other physical scenarios, such as supernova explosions or relativistic heavy-ion collisions [40]. More specifically, we have found this analogy to hold reasonably well when comparing our temperatures and entropies with the conditions encountered in the matter ejected in supernova explosions or in heavy-ion collisions at low energies, such as the ones to be produced in FAIR and NICA. On the other hand, both the supernova and the heavy-ion collision scenarios are not able to reproduce the extremely high baryon chemical potentials (i.e., $\mu_B > 1.5$ GeV, equivalent to more than 10 times saturation density) that can be achieved in neutron-star mergers. In this way, neutron-star mergers can provide a unique piece to the understanding of matter at extreme conditions of density and temperature.

As a concluding remark, we note that soon after our results were presented [5], Aloy et. al. [75] presented interesting results from a systematic investigation of the convexity of equations of state (EOSs)¹. In particular, they showed that non-convex thermodynamics, which can appear if the adiabatic index decreases sufficiently rapidly with increasing density, can affect the equilibrium structure of stable compact stars, as well as the dynamics of

¹ We recall that fluids following convex EOSs are such that their fluid elements increase their specific volume and decrease their pressure when overtaken by a rarefaction wave (i.e., rarefaction waves are “expansive”); similarly, they are compressed when overtaken by a compression wave (i.e., compression waves are “compressive”). Conversely, fluids following non-convex equations of state are such that their fluid elements behave rather “anomalously”, that is, they are compressed by rarefaction waves and rarefied by compression waves [53].

unstable neutron stars. In the latter case, a compression shock can be formed at the inner border of the convex region and affect the gravitational collapse to a black hole, leaving imprints on gravitational waveforms, which would be of increased amplitude [75]. This result was shown to hold when using our Chiral Mean Field (CMF) EOS, but also other EOSs that did not include a deconfinement phase transition. More importantly, it was found in Ref. [75] that those EOSs developing non-convex thermodynamics without a deconfinement first-order phase transition had a non-consistent treatment of matter constituents (non-relativistic instead of relativistic) or used specific sets of parameter in their relativistic mean-field approach that resulted in unphysical properties. A similar conclusion has been drawn by Schneider et. al in Ref. [76], who found that a pion-condensation transition does not mimic a quark deconfinement phase transitions, as it is usually less extreme and does not generate a second neutrino burst in supernova explosions. When taken together, these arguments strengthen our conclusion that a deconfinement phase transition can indeed leave distinguishable observable signals in different stages of neutron-star evolution.

Acknowledgements

Support for this research comes in part from PHAROS (COST Action CA16214), the LOEWE-Program in HIC for FAIR, the European Union’s Horizon 2020 Research and Innovation Programme (Grant 671698; call FETHPC-1-2014, project ExaHyPE), the ERC Synergy Grant “Black-HoleCam: Imaging the Event Horizon of Black Holes” (Grant No. 610058), and the National Science Foundation under grant PHY-1748621. HS also acknowledges the Judah M.-Eisenberg-Laureatus Professorship at the Fachbereich Physik at Goethe University. The simulations were performed on the SuperMUC cluster at the LRZ in Garching, on the LOEWE cluster in CSC in Frankfurt, and on the HazelHen cluster at the HLRS in Stuttgart.

References

1. L. Rezzolla, P. Pizzochero, I. D. Jones, N. Rea, and I. Vidaña, eds., *The Physics and Astrophysics of Neutron Stars*, Astrophysics and Space Science Library, Vol. 457 (2018).
2. L. Baiotti and L. Rezzolla, Rept. Prog. Phys. **80**, 096901 (2017), arXiv:1607.03540 [gr-qc] .
3. V. Paschalidis, Classical and Quantum Gravity **34**, 084002 (2017), arXiv:1611.01519 [astro-ph.HE] .
4. R. Oechslin, K. Uryū, G. S. Poghosyan, and F. K. Thielemann, Mon. Not. Roy. Astron. Soc. **349**, 1469 (2004), arXiv:astro-ph/0401083 [astro-ph] .
5. E. R. Most, L. J. Papenfort, V. Dexheimer, M. Hanauske, S. Schramm, H. Stöcker, and L. Rezzolla, Physical Review Letters **122**, 061101 (2019), arXiv:1807.03684 [astro-ph.HE] .

6. A. Bauswein, N.-U. F. Bastian, D. B. Blaschke, K. Chatziioannou, J. A. Clark, T. Fischer, and M. Oertel, *Phys. Rev. Lett.* **122**, 061102 (2019), arXiv:1809.01116 [astro-ph.HE] .
7. L. Baiotti, *Progress in Particle and Nuclear Physics* **109**, 103714 (2019), 1907.08534 .
8. Y. Sekiguchi, K. Kiuchi, K. Kyutoku, and M. Shibata, *Phys. Rev. Lett.* **107**, 211101 (2011), arXiv:1110.4442 [astro-ph.HE] .
9. D. Radice, S. Bernuzzi, W. Del Pozzo, L. F. Roberts, and C. D. Ott, *Astrophys. J. Lett.* **842**, L10 (2017), arXiv:1612.06429 [astro-ph.HE] .
10. A. Bauswein, H.-T. Janka, R. Oechslin, G. Pagliara, I. Sagert, J. Schaffner-Bielich, M. M. Hohle, and R. Neuhäuser, *Phys. Rev. Lett.* **103**, 011101 (2009), arXiv:0812.4248 .
11. G. Montaña, L. Tolós, M. Hanauske, and L. Rezzolla, *Phys. Rev. D* **99**, 103009 (2019), arXiv:1811.10929 [astro-ph.HE] .
12. C. Zhang, arXiv e-prints , arXiv:1908.10355 (2019), arXiv:1908.10355 [astro-ph.HE] .
13. R. De Pietri, A. Drago, A. Feo, G. Pagliara, M. Pasquali, S. Traversi, and G. Wiktorowicz, *Astrophys. J.* **881**, 122 (2019), arXiv:1904.01545 [astro-ph.HE] .
14. H. Gieg, T. Dietrich, and M. Ujevic, arXiv e-prints , arXiv:1908.03135 (2019), arXiv:1908.03135 [gr-qc] .
15. C. Ecker, M. Järvinen, G. Nijs, and W. van der Schee, arXiv e-prints , arXiv:1908.03213 (2019), arXiv:1908.03213 [astro-ph.HE] .
16. N. Bucciantini, A. Drago, G. Pagliara, and S. Traversi, arXiv e-prints , arXiv:1908.02501 (2019), arXiv:1908.02501 [astro-ph.HE] .
17. .
18. P. Papazoglou, D. Zschesche, S. Schramm, J. Schaffner-Bielich, H. Stoecker, and W. Greiner, *Phys. Rev.* **C59**, 411 (1999), arXiv:nucl-th/9806087 [nucl-th] .
19. V. Dexheimer and S. Schramm, *Astrophys. J.* **683**, 943 (2008), arXiv:0802.1999 [astro-ph] .
20. V. A. Dexheimer and S. Schramm, *Phys. Rev.* **C81**, 045201 (2010), arXiv:0901.1748 [astro-ph.SR] .
21. C. Ratti, M. A. Thaler, and W. Weise, *Proceedings, 18th International Conference on Ultra-Relativistic Nucleus-Nucleus Collisions (Quark Matter 2005): Budapest, Hungary, August 4-9, 2005*, *Rom. Rep. Phys.* **58**, 13 (2006).
22. S. Roessner, C. Ratti, and W. Weise, *Phys. Rev.* **D75**, 034007 (2007), arXiv:hep-ph/0609281 [hep-ph] .
23. J. Roark and V. Dexheimer, *Phys. Rev.* **C98**, 055805 (2018), arXiv:1803.02411 [nucl-th] .
24. N. K. Glendenning, *Phys. Rev.* **D46**, 1274 (1992).
25. B. Lukacs, J. Zimanyi, and N. L. Balazs, *Phys. Lett.* **B183**, 27 (1987).
26. U. W. Heinz, K. S. Lee, and M. J. Rhoades-Brown, *Mod. Phys. Lett.* **A2**, 153 (1987).
27. R. Poberezhnyuk, V. Vovchenko, M. I. Gorenstein, and H. Stoecker, *Phys. Rev.* **C99**, 024907 (2019), arXiv:1810.07640 [hep-ph] .
28. M. Hempel, V. Dexheimer, S. Schramm, and I. Iosilevskiy, *Phys. Rev.* **C88**, 014906 (2013), arXiv:1302.2835 [nucl-th] .
29. Y. Aoki, G. Endrodi, Z. Fodor, S. D. Katz, and K. K. Szabo, *Nature* **443**, 675 (2006), arXiv:hep-lat/0611014 [hep-lat] .
30. J. Steinheimer and S. Schramm, *Phys. Lett.* **B736**, 241 (2014), arXiv:1401.4051 [nucl-th] .
31. V. Dexheimer, R. de Oliveira Gomes, S. Schramm, and H. Pais, *Journal of Physics G Nuclear Physics* **46**, 034002 (2019), arXiv:1810.06109 [nucl-th] .
32. B. P. Abbott, R. Abbott, T. D. Abbott, F. Acernese, K. Ackley, C. Adams, T. Adams, P. Addesso, R. X. Adhikari, V. B. Adya, and et al. (LIGO Scientific Collaboration and Virgo Collaboration), *Phys. Rev. Lett.* **119**, 161101 (2017), arXiv:1710.05832 [gr-qc] .
33. E. Annala, T. Gorda, A. Kurkela, and A. Vuorinen, *Phys. Rev. Lett.* **120**, 172703 (2018), arXiv:1711.02644 [astro-ph.HE] .
34. A. Bauswein, O. Just, H.-T. Janka, and N. Stergioulas, *Astrophys. J. Lett.* **850**, L34 (2017), arXiv:1710.06843 [astro-ph.HE] .
35. B. Margalit and B. D. Metzger, *Astrophys. J. Lett.* **850**, L19 (2017), arXiv:1710.05938 [astro-ph.HE] .
36. D. Radice, A. Perego, F. Zappa, and S. Bernuzzi, *Astrophys. J. Lett.* **852**, L29 (2018), arXiv:1711.03647 [astro-ph.HE] .
37. L. Rezzolla, E. R. Most, and L. R. Weih, *Astrophys. J. Lett.* **852**, L25 (2018), arXiv:1711.00314 [astro-ph.HE] .
38. M. Ruiz, S. L. Shapiro, and A. Tsokaros, *Phys. Rev. D* **97**, 021501 (2018), arXiv:1711.00473 [astro-ph.HE] .
39. M. Shibata, S. Fujibayashi, K. Hotokezaka, K. Kiuchi, K. Kyutoku, Y. Sekiguchi, and M. Tanaka, *Phys. Rev. D* **96**, 123012 (2017), arXiv:1710.07579 [astro-ph.HE] .
40. E. R. Most, L. R. Weih, L. Rezzolla, and J. Schaffner-Bielich, *Phys. Rev. Lett.* **120**, 261103 (2018), arXiv:1803.00549 [gr-qc] .
41. V. Dexheimer, *Publications of the Astronomical Society of Australia* **34**, e066 (2017), arXiv:1708.08342 [astro-ph.HE] .
42. S. Typel, M. Oertel, and T. Klähn, *Physics of Particles and Nuclei* **46**, 633 (2015).
43. “Compose website,” <https://compose.obspm.fr/>.
44. Z. B. Etienne, V. Paschalidis, R. Haas, P. Mösta, and S. L. Shapiro, *Class. Quantum Grav.* **32**, 175009 (2015), arXiv:1501.07276 [astro-ph.HE] .
45. F. Löffler, J. Faber, E. Bentivegna, T. Bode, P. Diener, R. Haas, I. Hinder, B. C. Mundim, C. D. Ott, E. Schnetter, G. Allen, M. Campanelli, and P. Laguna, *Class. Quantum Grav.* **29**, 115001 (2012), arXiv:1111.3344 [gr-qc] .
46. D. Hilditch, S. Bernuzzi, M. Thierfelder, Z. Cao, W. Tichy, and B. Brügmann, *Phys. Rev. D* **88**, 084057 (2013), arXiv:1212.2901 [gr-qc] .
47. S. Bernuzzi and D. Hilditch, *Phys. Rev. D* **81**, 084003 (2010), arXiv:0912.2920 [gr-qc] .

48. D. Alic, C. Bona-Casas, C. Bona, L. Rezzolla, and C. Palenzuela, *Phys. Rev. D* **85**, 064040 (2012), arXiv:1106.2254 [gr-qc] .
49. D. Alic, W. Kastaun, and L. Rezzolla, *Phys. Rev. D* **88**, 064049 (2013), arXiv:1307.7391 [gr-qc] .
50. Y. Zlochower, J. G. Baker, M. Campanelli, and C. O. Lousto, *Phys. Rev. D* **72**, 024021 (2005), gr-qc/0505055 .
51. A. Weyhausen, S. Bernuzzi, and D. Hilditch, *Phys. Rev. D* **D85**, 024038 (2012), arXiv:1107.5539 [gr-qc] .
52. M. Alcubierre, *Introduction to 3 + 1 Numerical Relativity* (Oxford University Press, Oxford, UK, 2008).
53. L. Rezzolla and O. Zanotti, *Relativistic Hydrodynamics* (Oxford University Press, Oxford, UK, 2013).
54. L. Del Zanna, O. Zanotti, N. Bucciantini, and P. Londrillo, *Astron. Astrophys.* **473**, 11 (2007), arXiv:0704.3206 .
55. A. Harten, P. D. Lax, and B. van Leer, *SIAM Rev.* **25**, 35 (1983).
56. R. Borges, M. Carmona, B. Costa, and W. Don, *Journal of Computational Physics* **227**, 3191 (2008).
57. W. Kastaun, R. Ciolfi, and B. Giacomazzo, *Phys. Rev. D* **94**, 044060 (2016), arXiv:1607.02186 [astro-ph.HE] .
58. M. Hanauske, K. Takami, L. Bovard, L. Rezzolla, J. A. Font, F. Galeazzi, and H. Stöcker, *Phys. Rev. D* **96**, 043004 (2017), arXiv:1611.07152 [gr-qc] .
59. M. Hanauske, J. Steinheimer, A. Motornenko, V. Vovchenko, L. Bovard, E. R. Most, L. J. Papenfort, S. Schramm, and H. Stöcker, *Particles* **2**, 44 (2019).
60. M. Hanauske, L. Bovard, E. Most, J. Papenfort, J. Steinheimer, A. Motornenko, V. Vovchenko, V. Dexheimer, S. Schramm, and H. Stöcker, *Universe* **5** (2019), 10.3390/universe5060156.
61. A. Perego, S. Bernuzzi, and D. Radice, *Eur. Phys. J.* **A55**, 124 (2019), arXiv:1903.07898 [gr-qc] .
62. I. Bouras, E. Molnar, H. Niemi, Z. Xu, A. El, O. Fochler, C. Greiner, and D. H. Rischke, *Phys. Rev. Lett.* **103**, 032301 (2009), arXiv:0902.1927 [hep-ph] .
63. I. Bouras, E. Molnar, H. Niemi, Z. Xu, A. El, O. Fochler, C. Greiner, and D. H. Rischke, *Phys. Rev.* **C82**, 024910 (2010), arXiv:1006.0387 [hep-ph] .
64. A. Burrows and J. M. Lattimer, *Astrophys. J.* **270**, 735 (1983).
65. M. Prakash, I. Bombaci, M. Prakash, P. J. Ellis, J. M. Lattimer, and R. Knorren, *Phys. Rep.* **280**, 1 (1997), arXiv:nucl-th/9603042 .
66. S. Reddy, M. Prakash, and J. M. Lattimer, *Phys. Rev.* **D58**, 013009 (1998), arXiv:astro-ph/9710115 [astro-ph] .
67. C. Shen, U. Lombardo, N. Van Giai, and W. Zuo, *Phys. Rev.* **C68**, 055802 (2003), arXiv:nucl-th/0307101 [nucl-th] .
68. A. Pastore, M. Martini, D. Davesne, J. Navarro, S. Goriely, and N. Chamel, *Phys. Rev.* **C90**, 025804 (2014), arXiv:1408.2811 [nucl-th] .
69. T. Fischer, S. C. Whitehouse, A. Mezzacappa, F.-K. Thielemann, and M. Liebendörfer, *Astron. Astrophys.* **517**, A80 (2010), arXiv:0908.1871 [astro-ph.HE] .
70. L. Hüdepohl, B. Müller, H.-T. Janka, A. Marek, and G. G. Raffelt, *Phys. Rev. Lett.* **104**, 251101 (2010).
71. J. A. Pons, S. Reddy, M. Prakash, J. M. Lattimer, and J. A. Miralles, *Astrophys. J.* **513**, 780 (1999), astro-ph/9807040 .
72. T. Fischer, N.-U. F. Bastian, M.-R. Wu, P. Baklanov, E. Sorokina, S. Blinnikov, S. Typel, T. Klähn, and D. B. Blaschke, *Nature Astronomy* **2**, 980 (2018), arXiv:1712.08788 [astro-ph.HE] .
73. M. Hempel, G. Pagliara, and J. Schaffner-Bielich, *Phys. Rev.* **D80**, 125014 (2009), arXiv:0907.2680 [astro-ph.HE] .
74. A. Motornenko, V. Vovchenko, J. Steinheimer, S. Schramm, and H. Stöcker, *Nuclear Physics A* **982**, 891 (2019), the 27th International Conference on Ultrarelativistic Nucleus-Nucleus Collisions: Quark Matter 2018.
75. M. A. Aloy, J. M. Ibáñez, N. Sanchis-Gual, M. Obergaullinger, J. A. Font, S. Serna, and A. Miquina, *Mon. Not. R. Astron. Soc.* **484**, 4980 (2019), arXiv:1806.03314 [astro-ph.HE] .
76. A. S. Schneider, C. Constantinou, B. Muccioli, and M. Prakash, *Phys. Rev.* **C100**, 025803 (2019), arXiv:1901.09652 [nucl-th] .